Immersed Boundary Simulations of Flows Driven by Moving Thin Membranes

Marin Lauber[a,*], Gabriel D. Weymouth[a,b], Georges Limbert[a,c]

[a]*Faculty of Engineering and Physical Sciences, University of Southampton, UK*
[b]*Data-Centric Engineering Programme, Alan Turing Institute, UK*
[c]*Faculty of Health Sciences, University of Cape Town, South Africa.*

Abstract

Immersed boundary methods are extensively used for simulations of dynamic solid objects interacting with fluids due to their computational efficiency and modelling flexibility compared to body-fitted grid methods. However, thin geometries, such as shells and membranes, cause a violation of the boundary conditions across the surface for many immersed boundary projection algorithms. Using a one-dimensional analytical derivation and multi-dimensional numerical simulations, this manuscript shows that adjustment of the Poisson matrix itself is require to avoid large velocity, pressure, and force prediction errors when the pressure jump across the interface is substantial and that these errors increase with Reynolds number. A new minimal thickness modification is developed for the Boundary Data Immersion Method (BDIM-σ), which avoids these issues while still enabling the use of efficient projection algorithms for high-speed immersed surface simulations.

Keywords:

Immersed boundary method, Direct-forcing, Cartesian grid, Shell,

*Corresponding author
Email address:* `M.Lauber@soton.ac.uk` (Marin Lauber)

1. Introduction

Immersed boundary methods are a commonly used approach in computational fluid dynamics to simulate flow in complex domains or with moving or deforming boundaries [1, 2]. By solving the governing equations on a static Cartesian grid, mesh updates and/or re-meshing are completely avoided, rendering those methods highly efficient, at least from a computational point of view. However, imposing the correct boundary condition is less trivial than in body-fitted methods. Numerous methods have been developed to impose those boundary conditions on the body (see [3] for a thorough review), and in the following, we will use the term *immersed boundary method* to refer to these methods in general. The original Immersed Boundary method (IB) [4] uses a regularized Dirac delta function forcing to spread the reaction force of the body (obtained from a constitutive law) from the Lagrangian points onto the fluid. While this approach has been successful at simulating fluid-structure interaction cases consisting of a flexible body dominated by the flow advection [5], the method can lead to poor mass conservation near the body [6], resulting in a fluid leak across the interface [7]. This leakage was identified as being the result of a divergent interpolated velocity field that drives the Lagrangian points. Ways of improving this volume conservation by constructing divergence-free interpolated velocity field have been derived, see Bao et al. [8].

The immersed boundary can also be considered in a purely discretized setting, where it is explicitly defined to enforce the appropriate boundary

condition onto the body, as in the Direct-forcing method [9, 10]. The schemes that are used to reconstruct the velocity field in the vicinity of the immersed body are key to the accuracy of this method. For example, Fadlun et al. [10] showed that volume-averaged forcing only results in 1st-order convergence of the velocity field, while linear interpolation improves the results with 2nd-order convergence. In addition to the velocity field adjustment, Balaras [11] shows that Direct-forcing interpolation on a stationary body *implicitly* imposes a consistent homogeneous Neumann boundary condition onto the pressure-correction. However, immersed boundary methods are typically applied to moving geometries and unsteady simulations where the equations are solved using a fractional step algorithm [12], and in this case, the projection step introduces a slip error onto the velocity field [10, 13, 14, 15]. In the case of thin shells, this error is significant [16] and methods have been derived to reduce it, however, they are not able to completely remove it.

Another class of immersed boundary methods adjust the pressure equation in addition to the velocity field during the fractional step update. The Boundary Data Immersion Method (BDIM) [17, 18] explicitly adjusts the Poisson matrix such that the Neumann boundary condition on the pressure is respected on the immersed body. The resulting Poisson system has spatially varying coefficients, but it is otherwise unchanged. In these cases, standard linear algebra methods can be used to determine the pressure efficiently. Alternatively, the influence of the immersed boundary on the pressure field can be treated as an additional Lagrange multiplier as in the Immersed Boundary Projection Method (IBPM)[13, 19]. Including this additional constraint into the Poisson equation results in an augmented system whose solution ensures

imposition of the correct boundary condition on the velocity and pressure fields at the cost of solving a non-standard coupled Poisson problem.

In this work, we will show that when the immersed body is thin and dynamic, as is the case in many fluid-structure interaction problems (parachutes, insects wing, sail, heart valves, etc.), the lack of explicit boundary conditions on the pressure results in violation of both the pressure and velocity boundary conditions and therefore produces an erroneous solution. In cases where the pressure jump across the thin body is the dominant contribution to the overall force experienced by the body, the error is significant, and leads to large force prediction errors. Section 2 will use a simple one-dimensional (1D) example to illustrate that correcting this error requires explicit modification of the Poisson projection step. This careful analysis allows us to specify a set of mandatory numerical conditions for any Immersed Boundary method to successfully simulate problems involving thin dynamic surfaces. Section 3 will generalize this finding to 2D and 3D simulations of the Navier-Stokes equations, showing that the error increases with Reynolds number. In Section 3.3 we develop a modified approach termed BDIM-σ that allows for an efficient and accurate treatment of thin dynamic surfaces. Sections 4, 5 and 6 verify and validate the new approach and compare against existing Immersed Boundary methods for 2D and 3D flows generated by thin membranes including an oscillating thin shell, an impulsively accelerated circular disk, and a flapping insect wing.
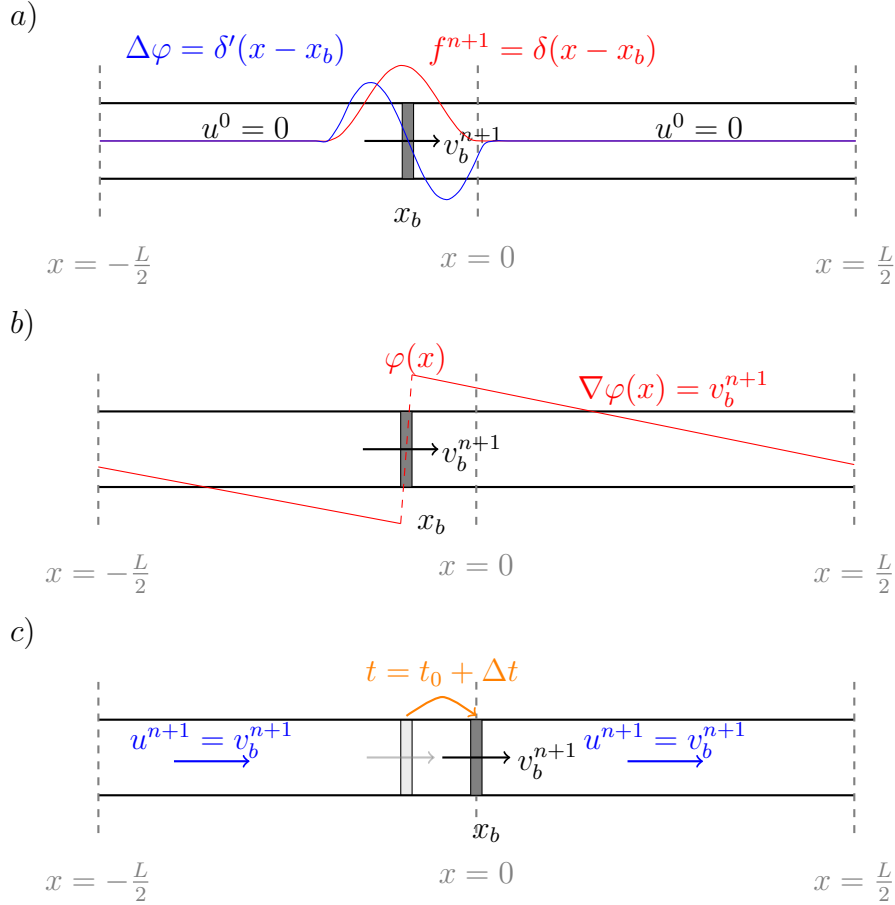
Figure 1: Schematic of the 1D periodic pipe with piston problem. The problem is periodic such that any quantity θ respects $\theta(x = -L/2) = \theta(x = L/2)$. The thin wall piston is initially located at $x = x_b$. The immersed forces f^{n+1} is added to the initial quiescent fluid field in $a)$. This immersed forcing generated a dipole source term for the pressure Poisson equation $a)$. The resulting pressure field after successful inversion of the Poisson equation with the correct f_p in $b)$. The final velocity field with the piston in its new position in $c)$.

2. Illustrative one-dimensional model

We start by demonstrating the errors introduced by incorrect pressure treatment in immersed boundary methods using a simple unsteady 1D-piston problem with an analytical solution. This is a simplification of the full 3D flow, which ignores the cross-section variation to focus on the driving impulse of the piston on the fluid. This simple system will allow us to directly compare the performance of a variety of immersed boundary methods.

2.1. Problem definition

We consider the flow inside a periodic 1D domain, in which a thin-wall piston is immersed, Figure 1. The flow and the piston inside the domain are initially quiescent, and the piston body has unsteady velocity $v_b(t)$ where $v_b(0) = 0$. The flow is assumed to be incompressible and viscous effects with the wall are omitted. The momentum equation in the direction of motion x is then simply

$$\frac{\partial u}{\partial t} = -\frac{1}{\rho}\frac{\partial p}{\partial x}, \tag{1}$$

where u, p are the 1D velocity and pressure fields and ρ is the constant fluid density. Velocity continuity is simply

$$\frac{\partial u}{\partial x} = 0. \tag{2}$$

This is complemented with adequate boundary conditions on the velocity and pressure fields at the piston location x_b

$$u(x_b, t) = v_b(t), \tag{3a}$$

$$\frac{\mathrm{d}p}{\mathrm{d}x}\bigg|_{x_b} = -\rho\frac{\mathrm{d}v_b}{\mathrm{d}t}. \tag{3b}$$

6

The solution at time t must be $u(x, t) = v_b(t)$ in order to satisfy continuity (2) and the velocity boundary condition (3a).

2.2. Immersed boundary formulation and solution

We demonstrate the necessity to correctly impose (3b) to solve this simple problem. Immersed boundary algorithms generally re-write equation (1, 2) in the form of a momentum update and pressure Poisson equation to obtain the solution at $t^{n+1} = t^n + \Delta t$ from the solution at t^n

$$u^{n+1} = u^n + r_{\Delta t}(u^n) - \frac{\Delta t}{\rho} \nabla p^{n+1} + f^{n+1} \tag{4a}$$

$$\nabla \cdot \left(\frac{\Delta t}{\rho} \nabla p^{n+1} \right) = \nabla \cdot \left(u^n + r_{\Delta t}(u^n) + f^{n+1} \right) \tag{4b}$$

where the term $r_{\Delta t}$ contains all the convective and viscous terms (which do not appear in this 1D example). The time level of the pressure term has been discussed in [20, 21, 22].

The forcing f^{n+1} in equations (4a,4b) enforces the velocity and pressure boundary conditions (3a,3b) from time t^n to t^{n+1}. In general, this forcing term can be a function of both the body velocity v_b and the fluid state u, p. This forcing is constrained to be local to the body, the piston position x_b in this case, using a Dirac delta function

$$f^{n+1} = \delta(x - x_b)C(v_b, u, p) \tag{5}$$

for some function $C(v_b, u, p)$ that imposes the boundary conditions, see Figure 1a. Since the fluid is initially still and letting $\varphi = \Delta t p^{n+1}/\rho$, we seek a solution to

$$\nabla^2 \varphi = \nabla \cdot f^{n+1} = \nabla \cdot \delta(x - x_b)C(v_b, u, p). \tag{6}$$

7

Because the Poisson equation is linear, we can split the function C in two functions, one for the velocity boundary condition $f_u = f_u(v_b, u)$ and one for the pressure boundary condition $f_p = f_p(v_b, p)$.

$$\nabla^2 \varphi = \delta'(x - x_b) f_u + \delta'(x - x_b) f_p + \delta(x - x_b) f_p', \tag{7}$$

where the last term appears due to the spatial dependency of the pressure boundary condition. Using the definition of the Dirac delta function as the derivative of the Heaviside function $\nabla H(x - x_b) = \delta(x - x_b)$, the solution to (7) is

$$\varphi = H(x - x_b)(f_u + f_p) + \nabla^{-2} \delta(x - x_b) f_p', \tag{8}$$

where ∇^{-2} is the inverse Laplacian. This solution is illustrated in Figure 1b, which shows the jump in the pressure across the piston body due to the Heaviside function, while the pressure boundary condition imposes the constant pressure gradient in the rest of the periodic domain.

The velocity field is simply

$$u^{n+1} = f^{n+1} - \nabla \varphi = -\nabla \nabla^{-2} \delta(x - x_b) f_p', \tag{9}$$

where the f^{n+1} terms cancel, revealing that the solution depends *only* on the treatment of the pressure boundary condition for this canonical problem. Note that the final velocity field satisfies condition (3a) as long as the pressure condition (3b) is met, since substituting (3b) into the time integrated governing equation (1) gives (3a).

2.3. Forcing terms with and without a pressure boundary condition

Table 1 summarizes six immersed boundary approaches and their accuracy when applied to this canonical test case (found online at [24]). The previous section showed that the forcing f^{n+1} must explicitly contain a term that

8

Table 1: Classification of the different immersed boundary methods and associated error on the 1D problem for zero thickness body. Error is quantified as $L_\infty(u^{n+1}/v_b^{n+1} - 1)$.

Method	Reference	Error
IB	[4]	0.9375
cIBM	[23]	0.9717
Direct-forcing	[10]	0.9375
BDIM	[18]	0.7239
IBPM	[19]	1.483×10^{-11}
BDIM-σ	-	3.306×10^{-10}

deals with the pressure boundary condition for problems which are pressure-driven, such as this piston flow. As such, the methods which do not include p^{n+1} in f^{n+1} (IB, cIBM, and Direct-forcing) show approximately 100% error in their solution.

BDIM and the new BDIM-σ approach presented in this manuscript use an update of the form

$$f^{n+1} = (1 - \mu^0) \left[v_b^{n+1} - u^n - r_{\Delta t}(u^n) + \frac{\Delta t}{\rho} \nabla p^{n+1} \right] \qquad (10)$$

where $1 - \mu^0 \sim \delta(x - x_b)$ is a kernel function centered on the body. The first term imposes (3a) on the body, while the second and third terms adjust the convection/diffusion and pressure forcing applied to the fluid close to the body. With the piston initially at rest, the pressure equation becomes

$$\nabla \cdot \frac{\mu^0 \Delta t}{\rho} \nabla p^{n+1} = \nabla \cdot (1 - \mu^0) v_b^{n+1}. \qquad (11)$$

where we can see that the addition of the pressure term in f^{n+1} has resulted in a Poisson equation with variable coefficients. If these coefficients

9

are properly developed, they enforce the pressure boundary condition and allow a jump in pressure across the interface, leading to the correct solution. As detailed in the next section, this requires a modification to BDIM for very thin geometries, which we call BDIM-σ. The error is reduced to machine precision using this approach.

The IBPM method also obtains good results on this problem but it requires a coupled momentum/pressure equation

$$\nabla^2 \lambda = \nabla \cdot r_1, \tag{12}$$

where $\lambda \equiv [\frac{\Delta t}{\rho} p^{n+1}, f_u]^\top$ and $r_1 = [0, v_b^{n+1}]^\top$, such that the pressure and the velocity forcing are determined simultaneously to enforce both the no-slip and the divergence-free constraint. The primary methodological contribution of this manuscript is that BDIM-σ achieves this high level of accuracy while using a standard Poisson equation.

3. A minimal thickness Boundary Data Immersion Method

The previous section illustrates that the projection step must explicitly impose the boundary condition on the pressure for the results to be accurate. This section generalizes that result for immersed surface simulations of the two and three dimensional Navier-Stokes equation. In particular, we demonstrate the requirement of a finite body thickness for the Boundary Data Immersion Method (BDIM) and develop a new approach to simulate the flow past thin surfaces.

As detailed in [18] BDIM solves a *meta*-equation for the velocity field $\vec{u}$ developed from a convolution of the Navier-Stokes equations in the fluid

10

domain Ω_f with the prescribed velocity in the body domain Ω_b. First we write the fluid equation in the form of an update over a time step $\Delta t = t^{n+1} - t^n$

$$\vec{u}(t^{n+1}, \vec{x}) = \vec{u}(t^n, \vec{x}) + \vec{r}_{\Delta t}(\vec{u}(t, \vec{x})) - \vec{\nabla} p_{\Delta t}(\vec{x}), \quad \forall \vec{x} \in \Omega_f, \tag{13a}$$

$$\vec{r}(\vec{u}) = \frac{1}{Re} \nabla^2 \vec{u} - \vec{u} \cdot \vec{\nabla} \vec{u}, \tag{13b}$$

154 where we use the notation $f_{\Delta t} = \int_{t^n}^{t^{n+1}} f \, \mathrm{d}t$ for the impulse of f across the time
155 step, $\vec{\nabla} p_{\Delta t}$ is the pressure impulse with $p \equiv P/\rho U^2$ the non-dimensionnal
156 pressure (U is a velocity length-scale), $\vec{r}_{\Delta t}$ is the impulse of all non-pressure
157 terms and Re is the Reynolds number. The body velocity update is simply:

$$\vec{u}(t^{n+1}, \vec{x}) = \vec{v}_b(t^{n+1}, \vec{x}), \quad \forall \vec{x} \in \Omega_b. \tag{14}$$

158 We can extend the domain of application of the fluid and the solid governing
159 equations onto the full domain $\vec{x} \in \Omega = \Omega_f \cup \Omega_b$ by convolution of the
160 equations using a kernel with support ϵ

$$\phi_\epsilon(|x - x'|) = \begin{cases} \frac{1}{2\epsilon} \left(1 + \cos\left(\frac{|x - x'| \pi}{\epsilon} \right) \right) & \text{if } |x - x'| < \epsilon \\ 0 & \text{else.} \end{cases} \tag{15}$$

161 Evaluation of this convolution using a Taylor series expansion up to second
162 order and assuming that the boundary can be approximated by its local
163 tangential plane we obtain an equation for the convolved velocity field $\vec{u}_\epsilon$
164 valid throughout the domain

$$\begin{aligned} \vec{u}_\epsilon^{n+1} = \mu^0 \left(\vec{u}_\epsilon^n + \vec{r}_{\Delta t}(\vec{u}_\epsilon^n) - \vec{\nabla} p_{\Delta t} \right) + (1 - \mu^0) \vec{v}_b \\ + \mu^1 \frac{\partial}{\partial n} \left(\vec{u}_\epsilon^n + \vec{r}_{\Delta t}(\vec{u}_\epsilon^n) - \vec{v}_b - \vec{\nabla} p_{\Delta t} \right), \end{aligned} \tag{16}$$

165 where we define $\mu^k(s) = \int_{-\epsilon}^{s} \phi_\epsilon(x) x^k \, \mathrm{d}x$ as the moments of the kernel and
166 $s(\vec{x}, t)$ is the signed distance function to the boundary $\partial \Omega_b$. See [18] for a

11

full derivation. The key properties of this meta-equation are (i) the kernel moments *smoothly* ramp between the fluid and solid governing equations, and (ii) this transition is applied not only to the velocity and convection/diffusion impulse $(u_\epsilon, v_b, r_{\Delta t})$ but *also* to the pressure impulse.

Equation 16 is solved using the fractional step method, where the pressure is determined by requiring that the final velocity field be divergence-free. Heun's method is use to integrate the equation form $\vec{u}^n = \vec{u}_\varepsilon(t^n)$ to find $\vec{u}^{n+1} = \vec{u}_\varepsilon(t^{n+1})$ in two steps, first an explicit Euler step is performed using $\vec{v}_b = \vec{v}_b(t^{n+1})$

$$\vec{u}^* = \mu^0 \left(\vec{u}^n + \vec{r}_{\Delta t}(\vec{u}^n) \right) + (1 - \mu^0)\vec{v}_b + \mu^1 \frac{\partial}{\partial n} \left(\vec{u}_\epsilon^n + \vec{r}_{\Delta t}(\vec{u}^n) - \vec{v}_b \right), \quad (17a)$$

$$\Delta t \vec{\nabla} \cdot \left(\mu^0 \vec{\nabla} p_0 \right) = \vec{\nabla} \cdot \vec{u}^*, \quad (17b)$$

$$\vec{u}_1 = \vec{u}^* - \Delta t \mu^0 \vec{\nabla} p_0, \quad (17c)$$

followed by Heun's corrector step

$$\vec{u}_1^* = \mu^0 \left(\vec{u}^n + \vec{r}_{\Delta t}(\vec{u}_1) \right) + (1 - \mu^0)\vec{v}_b + \mu^1 \frac{\partial}{\partial n} \left(\vec{u}_0 + \vec{r}_{\Delta t}(\vec{u}_1) - \vec{v}_b \right), \quad (18a)$$

$$\Delta t \vec{\nabla} \cdot \left(\mu^0 \vec{\nabla} p_2 \right) = \vec{\nabla} \cdot \vec{u}_1^*, \quad (18b)$$

$$\vec{u}_2 = \vec{u}_1^* - \Delta t \mu^0 \vec{\nabla} p_2, \quad (18c)$$

$$\vec{u}^{n+1} = \frac{1}{2}(\vec{u}_1 + \vec{u}_2), \quad (18d)$$

where all the impulses are approximated using explicit methods.

3.1. Pressure boundary condition enforcement

At a non-slip wall, the pressure can be shown to satisfy the condition

$$\frac{\partial p}{\partial n} = \hat{n} \cdot \left[-\rho \frac{\mathrm{D}\vec{v}_b}{\mathrm{D}t} + \mu \nabla^2 \vec{u} \right]. \quad (19)$$

174 where $\mathrm{D}\vec{v}_b/\mathrm{D}t$ is the acceleration of the moving wall. In this section we will

175 show that this condition can only be imposed by explicit modification of the

176 coefficients of the Poisson equation. We will use our 1D case to show that

177 in the limit of vanishing kernel width, our method imposes this boundary

178 condition on the pressure field implicitly. This argument extends to higher

179 dimensions.

180   The pressure is determined through the solution of the Poisson equation

181 in 17b. As opposed to other immersed methods, BDIM uses a *variable* coef-

182 ficient Poisson equation due to the kernel moment μ^0. A distance $\pm\epsilon$ from

183 the surface, the kernel moment ranges from $\mu^0(s \geq \epsilon) = 1$ outside the body

184 to $\mu^0(s \leq -\epsilon) = 0$ within the body. The influence of the pressure gradient

185 is removed when $\mu^0 = 0$, turning off the pressure sensitivity across the body

186 and enforcing the Neumman pressure condition.

187   We demonstrate this using the 1D example of the previous section since

188 the argument generalizes directly to the 2D and 3D cases. On a 1D uniform

189 grid, a finite volume integration over cell $\Delta\Omega_i$ and central difference of a

190 derivative at cell face $i + \frac{1}{2}$ gives

$$\int_{i-\frac{1}{2}}^{i+\frac{1}{2}} \frac{d\phi}{dx}\, \mathrm{d}x = \phi_{i+\frac{1}{2}} - \phi_{i-\frac{1}{2}} \quad \text{and} \quad \left.\frac{dp}{dx}\right|_{i+\frac{1}{2}} = \frac{p_{i+1} - p_i}{\Delta x}, \qquad (20)$$

191 where Δx is the uniform spacing. Substitution into Equation 17b gives the

192 discrete Poisson equation

$$\mu^0_{i+\frac{1}{2}}\, (p_{i+1} - p_i) - \mu^0_{i-\frac{1}{2}}\, (p_i - p_{i-1}) = \frac{\Delta x}{\Delta t}\left(u^*_{i+\frac{1}{2}} - u^*_{i-\frac{1}{2}}\right). \qquad (21)$$

193   Now, consider when the boundary $\partial\Omega_b$ is located at $i + \frac{1}{2}$. Letting the

194 support of the kernel $\epsilon \to 0$ such that $\mu^0_{i+\frac{1}{2}} = \mu^1_{i\pm\frac{1}{2}} = 0$ while $\mu^0_{i-\frac{1}{2}} = 1$ gives

13

a pressure Poisson equation

$$- (p_i - p_{i-1}) = \frac{\Delta x}{\Delta t} \left(v_b^{n+1} - u_{i-\frac{1}{2}}^* \right), \tag{22}$$

where $u_{i+\frac{1}{2}}^* = v_b^{n+1}$ from Equation 17a. This is *exactly* the Poisson equation we would obtain by substituting the velocity and pressure boundary condition (3a),(3b) into a constant coefficient ($\mu^0 = 1$ everywhere) Poisson equation at this boundary point. This is a 1D discretization of (19) where the viscous term has vanished due to the unidimensionality of the problem. This same argument applies to 2D and 3D Poisson equations as well; the pressure condition (19) is automatically applied to all immersed surfaces as $\mu^0 \to 0$ in the body. The zeros in the Poisson matrix ensure that condition (19) is imposed as we approach the body and that pressure jumps across the interface do not influence the fluid momentum on either side, which would result in an leakage of fluid across the body. The resulting linear system can still be solved with standard iterative methods (relaxation, Krylov subspace, Multi-Grid, etc), unlike IBPM which requires careful construction of the augmented system to ensure that it is positive-definite and well-conditioned [13].

3.2. Acceleration and Reynolds number dependence

We note that the error introduced by the lack of explicit boundary condition on the pressure field is dependent on the strength of the r.h.s of equation 17b. The major contributor to the magnitude of this source term in the Poisson equation is the local body acceleration (through the v_b^{n+1} term). However, the Reynolds number of the flow will also influence the strength of this source term. Low Reynolds number flow is characterized by a relatively
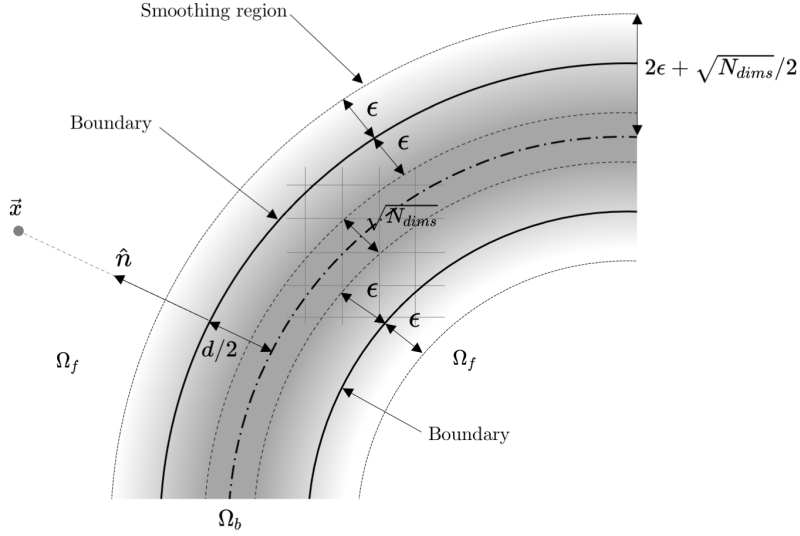
14

Smoothing region

$2\epsilon + \sqrt{N_{dims}}/2$

ϵ

ϵ

Boundary

$\vec{x}$

$\sqrt{N_{dims}}$

$\hat{n}$

ϵ

ϵ

Ω_f

$d/2$

Ω_f

Boundary

Ω_b

Figure 2: Schematic of the BDIM smoothing for a general thin 2D body. The smoothing occurs in a region ϵ away from the boundary, represented here by the gray gradient area. A schematic of a 2D grid is also depicted to show the minimum width of the core of the body (where $\mu^0 = 0$) that ensure the Neumann condition is respected.

smooth velocity gradient near walls compared to high Reynolds number flow, therefore reducing the contribution of $r_{\Delta t}$ to the source term. This means that the errors in immersed boundary methods which do not enforce the Neumann condition in the project step will be more severe as the Reynolds number increases, which may explain why this issue is not referenced more commonly in the literature of low Re immersed boundary simulations. We will demonstrate the magnitude and increasing severity of these errors with Re in Section 5.

3.3. BDIM-σ

227 We have shown that the Neumann condition is imposed for boundary cells

228 if $\mu^0 = 0$ within the body. With a kernel support of $\epsilon = 2\Delta x$, as suggested in

229 [18], the smoothing region on each side of a 1D body has a width of $4\Delta x$. If

230 the center of the body is aligned with a grid point, we would satisfy $\mu^0 = 0$ for

231 this point. In general, however, the body will not be aligned with a grid point

232 and we must increase the width of the central region of the μ^0 kernel moment

233 to ensure that this is true regardless of the position of the body. Therefore,

234 in 1D we must increase the body thickness to $5\Delta x$ to satisfy the requirement

235 and in N_{dims} we find that the minimum body thickness is $(4 + \sqrt{N_{dims}})\Delta x$,

236 Figure 2. This means that accurate predictions around very thin bodies in

237 3D space requires decreasing Δx at the cost of significantly more expensive

238 simulations.

239 In this section, we present BDIM-σ, a simple adjustment to the classic

240 BDIM method which enables the accurate simulation of thin bodies and

241 even $\mathbb{R}^2$ bodies (plates, shells, membranes) immersed in a $\mathbb{R}^3$ fluid domain. In

242 particular, we follow the common *slender body* formulation that parametrizes

243 a thin 3D body by a mid-plane surface σ and a local thickness d, see [25, 26].

244 In other words, the points on the body surface are defined as

$$\vec{x} \in \partial\Omega_b = \vec{\sigma}(\vec{\xi}) \pm \tfrac{1}{2}d(\vec{\xi})\hat{n}(\vec{\xi}) \tag{23}$$

245 where $\vec{\xi}$ are the curvilinear coordinates of the mid-surface and $\hat{n}$ is the unit

246 normal.

247 Our aim is to produce a zeroth kernel moment μ^0 which behaves similarly

248 to a top-hat function; rapidly but smoothly transitioning from 1 to 0 to 1

as we travel through an immersed geometry of any thickness, Figure 2. To achieve this, we first minimize the size of the smoothing region by setting $\epsilon = \Delta x/2$. This makes the meta-function transition more abrupt, but the following sections demonstrate that the results are still numerically stable and accurate. Second, we adjust the signed distance function to ensure that the flat $\mu^0 = 0$ section is always present, regardless of the body thickness d

$$s(\vec{x}, t) = s_\sigma(\vec{x}, t) - \max\left(\tfrac{1}{2} d(\vec{x}, t),\ C_1 \Delta x\right), \tag{24}$$

where s_σ the signed distance to the surface σ, $d(\vec{x}, t)$ is the local thickness at the normal projection point of $\vec{x}$, see Figure 2, and $C_1 = \tfrac{1}{2} + \tfrac{1}{2}\sqrt{N_{\mathrm{dims}}}$ is the minimum thickness coefficient which depends on the number of spatial dimensions N_{dims}. This new adjusted signed distance function ensures the proper boundary condition will be applied, even in the limit of a vanishing thickness, i.e. a $\mathbb{R}^2$ surface in $\mathbb{R}^3$ space. As $d \to 0$, the $\mu^0 = 0$ section extends outside the body the minimum amount required to maintain the modified Poisson equation.

4. Convergence Study: Oscillating Thin Shell

In this section we verify the numerical convergence of our implementation of BDIM-σ using the 2D test case of an oscillating circular shell in quiescent fluid, equivalent to the test used in [10] and presented in [27]. A thin shell of diameter D and thickness $d = D/16$ is placed in the center of a box of size $H = 8D$ filled with incompressible viscous fluid at rest. The inside of the shell also contains incompressible viscous fluid at rest, Figure 3b. Fluid flow is obtained by prescribed motion of the shell

$$x(t) = x_0 + A\left(1 - \cos(2\pi f t)\right), \quad y(t) = y_0, \tag{25}$$

17

271 where the amplitude of motion is $A = 0.125D$, the frequency $f = 1\ Hz$, and
272 $\vec{x}_0 = \vec{x}(t = 0)$ is the initial position of the shell. The Reynolds Number of
273 the flow is $Re = UD/\nu = 200$, where the reference velocity is $U = 2\pi f A$.

274   The simulations are performed using an in-house code, Lotus, that has
275 been validated for a wide range of flows at intermediate Reynolds numbers,
276 with and without immersed bodies [18, 28, 29, 30]. The governing equations
277 are solved on a Cartesian finite-volume mesh. The convective term is approx-
278 imated using a flux-limited Quadratic Upstream Interpolation for Convective
279 Kinematics (QUICK) [31] scheme for stability, and central difference is used
280 for the diffusive terms. Turbulence is modelled using implicit Large Eddy
281 Simulation (iLES) model that uses flux limiting to model the energy loss due
282 to sub-grid stress. The solution to the Poisson equation are obtained using
283 a multi-grid method. We use adaptive time-steps based on the convective
284 and diffusive Courant velocities. The second-order spatial and temporal con-
285 vergence of the flow solver without immersed boundaries is demonstrated on
286 the 2D Taylor-Green vortex in appendix Appendix A.

287   Simulations for the 2D oscillating shell problem are produce using four
288 uniform meshes of size $D/\Delta x \in [32, 64, 128, 256]$. Figure 3b shows a snap-
289 shot of the solution. The results show the expected internal and external
290 flow pattern and pressure field, including the discontinuous jump in pressure
291 across the thin shell wall. Quantitatively, the internal flow is captured per-
292 fectly, without any variations between mesh size, as the velocity field solution
293 is constant and the pressure is linear. As the motion amplitude is finite, a
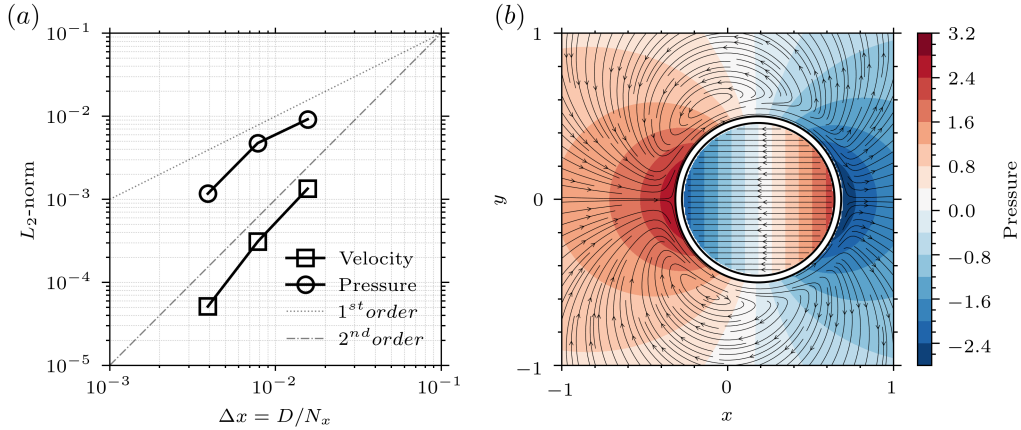294 closed-form solution for the external flow does not exist. As such, we use the

18

Figure 3: (a) Convergence in the L_2-norm of the pressure and velocity field. (b) pressure contour and velocity streamlines for the external and internal flow at $t = 0.5$. The internal flow follows rigid body motion.

results of the finest mesh to define the L_2-norm of the error for a variable φ

$$L_2^N(\varphi) = \left[\frac{1}{N^2} \sum_{i=1}^{N^2} |\varphi_i^N - \varphi_i^e|^2 \right]^{1/2} . \tag{26}$$

Figure 3a shows the second order-convergence (dashed-line) for the pressure $(p = 2.0)$ and velocity $(p = 2.0)$ field in the L_2-norm, verifying the numerical accuracy of the proposed BDIM-σ method.

5. Application: Accelerating Thin Disk

In this section we validate the performance of the new BDIM-σ approach compared to other immersed boundary methods on the pressure-driven flow around an impulsively accelerated thin circular disk. Following the experimental and numerical study presented in [29], an initially static circular disk with diameter D is accelerated from rest with constant acceleration a
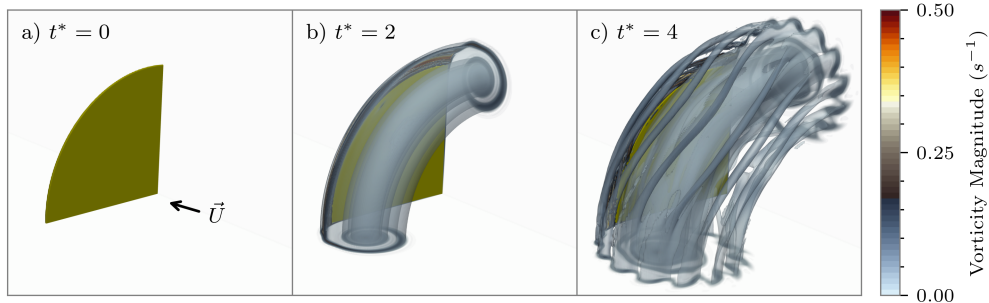
Figure 4: Time snapshot of the disk and the vortex structure visualized using the iso-surface of $\lambda_2 U^2/D^2 = -32$, coloured with vorticity magnitude $|\omega|U/D$. Disk and vortex core shown at initial impulse, end of acceleration phase, and in the steady phase. Only 1/4 of the disk and vortex core are shown. Animation of this figure is provided as supplementary material.

in a quiescent fluid up to a terminal velocity U, after which the velocity is held steady. Figure 4 visualizes the resulting flow for non-dimensional acceleration $a^* = aD/U^2 = 0.5$ at $t^* = tU/D = 0$, $t^* = 2$ (the end of acceleration), and $t^* = 4$. The Reynolds number at the terminal velocity is $Re = UD/\nu = 1.25 \times 10^5$.

We compare three different immersed boundary methods, a Direct-forcing method that uses linear velocity reconstruction [10], classic BDIM [18], and the new BDIM-σ developed above. As we are focused on the early development of the flow, we make use of the double symmetry of the geometry and wake to reduce the mesh count by simulating the flow over 1/4 of the disk. (The wake breaks symmetry only after $t^* > 20$ even at high Re [29].) The no-slip boundary condition is applied on the disk. A zero normal flux condition is applied at the exterior domain boundaries. A uniform grid region of $[1.25 \times 1.25 \times 1.25]$ disk radius is used to properly capture the vortex roll-up

20
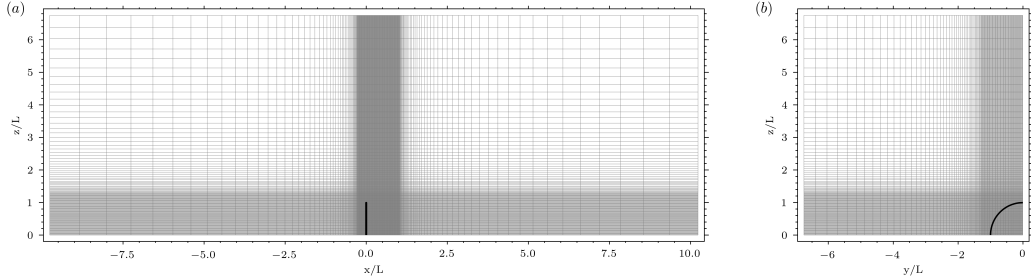
Figure 5: Profile and front view of the finest grid used for the thin circular disk case. The top view is identical to the profile view. For clarity every two cells are shown in each direction.

and the wake of the disk, see Figure 5. Grid stretching is used to fill the rest of the domain until it reaches the total size of $[20 \times 6.66 \times 6.66]$ disk radius. Instead of accelerating the disk itself, we accelerate the fluid inside the domain. This ensures that the wake is always located in the uniform region of the grid. Inlet boundary conditions are prescribed as $\vec{u} = [V(t), 0, 0]$, where $V(t) = at$ for $0 < t < U/a$ and $V(t) = U$ for $t \geq U/a$. A convective condition is applied at the domain exit plane downstream of the body.

We perform two convergence studies for the disk case; in the first one, we only vary the spatial resolution, and in the second one, we also vary the thickness of the body. Convergence is assessed by comparing the pressure impulse $I \equiv \int_0^T F/\rho D^2 \, dt^*$ where we have taken $T = 4t^*$ for all cases. Richardson extrapolation is used to obtain the extrapolated value and apparent order of convergence.

We obtain the expected 2nd-order convergence rate $(p = 1.82)$ in the case where only the numerical parameter Δx is varied, with relative errors close to 0.15% for the finest mesh, see Figure 6. Unsurprisingly, the convergence

21

(a)

(b)
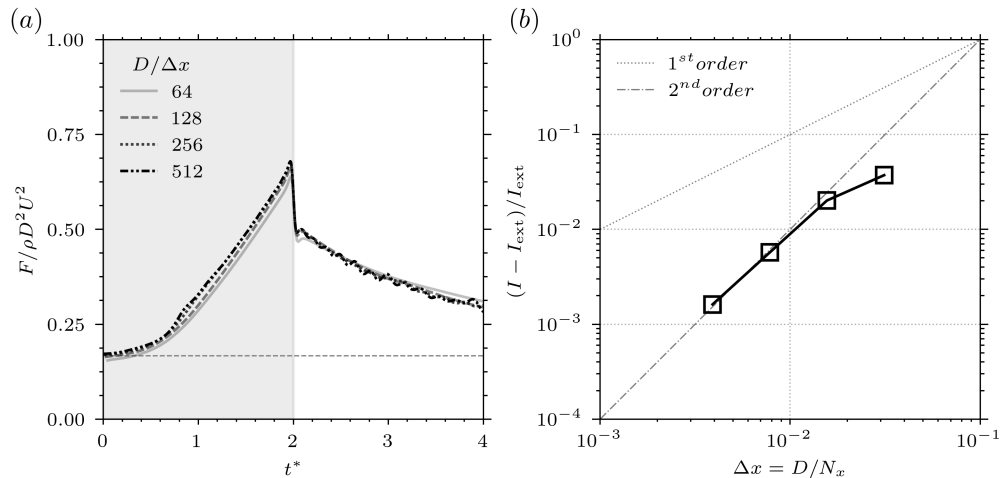
Figure 6: Convergence of the pressure impulse for the thin circular disk with constant thickness ratio $D/d = 32$ and varying resolution. (a) Normalized pressure force acting on the disk for varying resolution and (b) relative error in the pressure impulse to the Richardson extrapolated value.

behaviour changes when the body thickness is simultaneously reduced with the grid size, see Figure 7. However, the fine mesh results presented are still within 2% of the Richardson extrapolated value for $d \to 0$. We use the fine mesh for all the simulations presented hereafter.

5.1. Results

Our results focus on a single disk acceleration, $a^* = 0.5$, as the change in fluid response as a function of a^* is documented in the study by Fernando et al. [29]. In addition to testing the three immersed boundary methods, we also vary the disk thickness d for the BDIM and BDIM-σ methods to test the performance for very thin bodies. We use a constant $d/\Delta x = 4$ for the Direct-forcing method as the pressure BC is not enforced regardless of thickness.

22
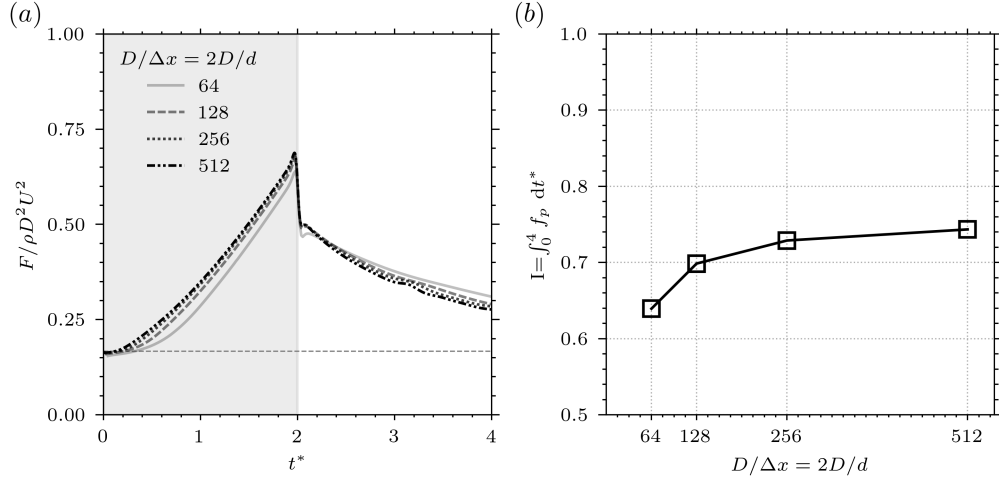
Figure 7: Thickness study for the thin circular disk with the thickness reduced simultaneously with the grid spacing, maintaining a minimal $d = 2\Delta x$ at each resolution. (a) normalized pressure force on the disk at various resolution, (b) variation of the pressure impulse for varying resolution and thicknesses.

Axial velocity profiles through the center-plane of the disk near the edge are shown on Figure 8. The profiles are taken at $t^* = 4$, which is during the steady motion phase. The solutions for Direct-forcing (with $d/\Delta x = 4$) and BDIM (when $d/\Delta x < 4$) are both seen to leak through the disk, violating the normal velocity condition. In contrast, BDIM-σ always enforces the velocity BC, letting us study the influence of changing disk thickness on the flow without this modelling error. We observe differences in the velocity profiles resulting in a different shear-layer behaviour, depending on the disk thickness. Thicker disks result in separation from the front corner in addition to the back, leading to a more complex velocity profile.

The resulting time history of the normalized pressure force acting on the disk can be seen on Figure 9. The initial added-mass force is compared to

23
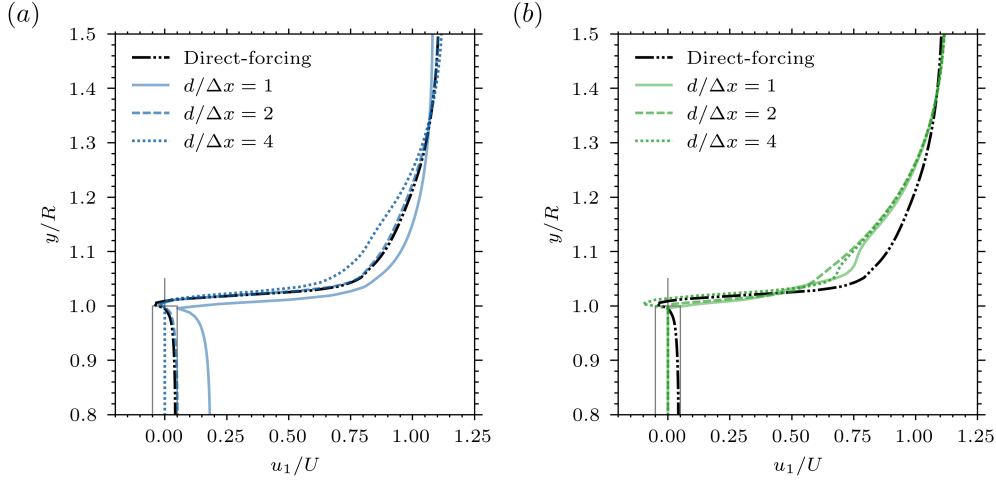
Figure 8: Axial (u_1) velocity profile on the top of the accelerated thin disk at a non-dimensional time $t^* = 4$ for (a) BDIM and Direct-forcing and (b) BDIM-σ and Direct-forcing. The thickness of the disk is exaggerated for visualisation purpose.

the analytical expression for the added-mass coefficient

$$C_a = \frac{F}{\rho D^3 a} = \left(\frac{F}{\rho D^2 U^2} \right) \frac{1}{a^*} = \frac{1}{3}, \tag{27}$$

from potential flow theory for a thin circular disk, see Brennen [32]. This value is shown as a horizontal dashed line in Figure 9 and the initial force predictions for each method are summarized in Table 2. The Direct-forcing method completely misses this initial added-mass force, while BDIM is able to capture the force accurately, provided the body is sufficiently thick ($d/\Delta x \geq$ 4). The new BDIM-σ method ensures the correct pressure boundary condition is always applied and so the initial force is always captured.

In addition to validating the initial impulse force with potential flow theory, we validate the force peak (F_{peak}) using published experimental data [29, 33]. The results are presented in Table 2. The experimental values are

24
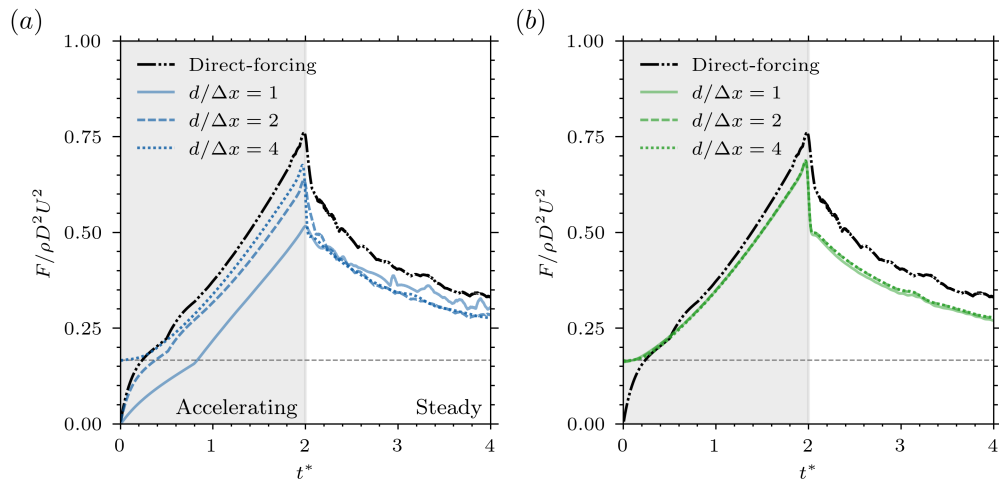
Figure 9: Normalized pressure force acting on an impulsively started disk (*a*) BDIM and Direct-forcing, (*b*) BDIM-σ and Direct-forcing for $a^* = 0.5$. Results are presented with various disk thicknesses (in terms of FV mesh spacing). The horizontal dashed line ($F/\rho D^2 U^2 = a^*/3$) represents the theoretical added-mass coefficient (only valid for the initial impulse). The accelerating ($v_b = at$) and steady phase ($v_b = U$) are represented by the gray and white shaded areas, respectively.

Table 2: Normalized initial and peak force at $U/U_{max} = 0$ and $U/U_{max} = 1$ for the different numerical methods and the experimental data. Numerical results are shown for the finest mesh with various thickness to diameter ratios d/D. The Direct-forcing results use $d/D = 4/512$. The relative error compared to the reference solution is also shown.

Method	d/D	F_{init}	%Error	F_{peak}	%Error
Direct-forcing [10]		0.012	96.4	1.52	14.4
BDIM	1/512	0.001	99.6	1.032	22.4
	2/512	0.010	97.1	1.272	4.36
	4/512	0.333	0.06	1.351	1.61
BDIM-σ	1/512	0.332	0.36	1.369	2.96
	2/512	0.332	0.26	1.375	3.42
	4/512	0.333	0.08	1.373	3.20
Reference	Analytical	1/3.	-	-	-
	Experimental [29, 33]	-	-	1.33 ± 0.02	-

$_{370}$ obtained for the same acceleration, but with $Re = 50 \times 10^3$. This difference

$_{371}$ in Re is not significant as Fernando et al. [29] shows the peak forces are very

$_{372}$ weakly sensitive to the Reynolds number and we confirm this in Figure 10.

$_{373}$ The experimental peak force is obtained from an average of the peak forces

$_{374}$ from 125 measurements with a disk of $d/D = 0.01$. The standard deviation of

$_{375}$ 1.3% is used as an estimate of the experimental uncertainty in this value. As

$_{376}$ before, Direct-forcing method has the largest error, although now the lack of

$_{377}$ pressure boundary condition has resulted in an *over*-estimate of the pressure

$_{378}$ force which continues through the steady velocity phase ($t^* > 2$). Table 2

$_{379}$ shows the classic BDIM method approaches (and overshoots) the peak ex-

$_{380}$ perimental drag as the thickness is increased. However, classic BDIM cannot

$_{381}$ enforce the pressure boundary condition exactly when $d/D = 1/512$ (corre-

$_{382}$ sponding to $d = 2\Delta x$) which results in more than 20% error. In contrast,

$_{383}$ BDIM-σ always enforces the pressure boundary condition and therefore gives

$_{384}$ an essentially constant force prediction within around 3% of the experiments

$_{385}$ even as $d \rightarrow 0$.

$_{386}$ Finally, we verify the arguments in Section 3 and show the increased

$_{387}$ importance of the pressure boundary condition with increased Re (Figure 10).

$_{388}$ The BDIM and BDIM-σ solution using $d/D = 4/512$ are indistinguishable

$_{389}$ and show very little change in the force profile as the Reynolds number is

$_{390}$ increased from $Re = 100$ to 1250 to 125000, especially during the acceleration

$_{391}$ phase ($t^* < 2$), in agreement with the experimental findings [29, 33]. In

$_{392}$ contrast, the Direct-forcing results only match BDIM and BDIM-σ for $Re =$

$_{393}$ 100, with large force errors at higher Re. The leakage observed and incorrect

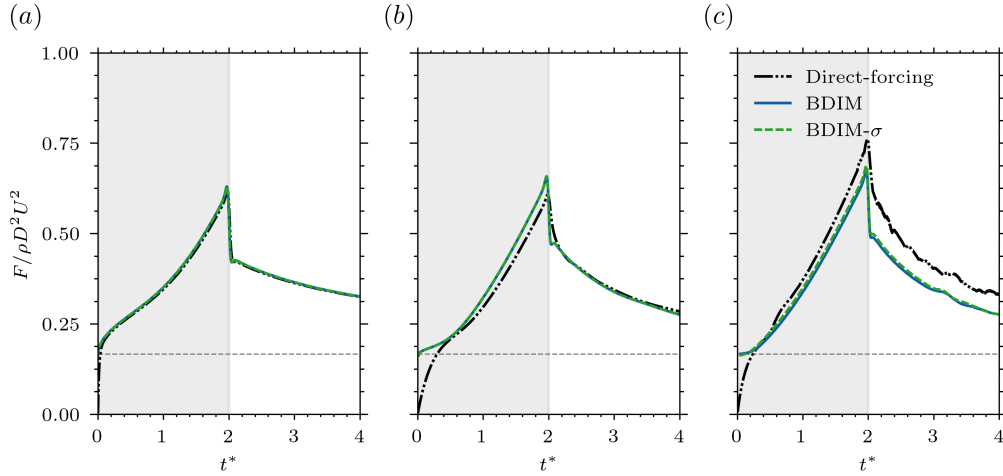$_{394}$ force predictions are purely due to the pressure field being computed without

Figure 10: Normalized pressure force acting on an impulsively started disk for the BDIM, BDIM-σ, and Direct-forcing method using $d/D = 4/512$ at Reynolds number, (a) 100, (b) 1250 and (c) 125×10^3 for $a^* = 0.5$. The horizontal dashed line ($F/\rho D^2 U^2 = a^*/3$) represents the theoretical added-mass coefficient (only valid for the initial impulse).

proper boundary conditions on the body. This results in a non-zero pressure flux across the disk during the projection step, and this error is exaggerated as the flow gradients near the boundary increase, i.e. at higher Re. The only way to avoid this issue for all Re is to adjust the Poisson equation for the pressure such that the Neumann boundary condition is imposed explicitly.

6. Application: Flapping Insect Wing

As a final example, we consider the flow induced by a flapping insect wing, demonstrating the performance of immersed boundary methods when modelling moving three-dimensional thin structures. The geometry is a simplified representation of a *drosophila* wing (a common fly), commonly modeled as

28
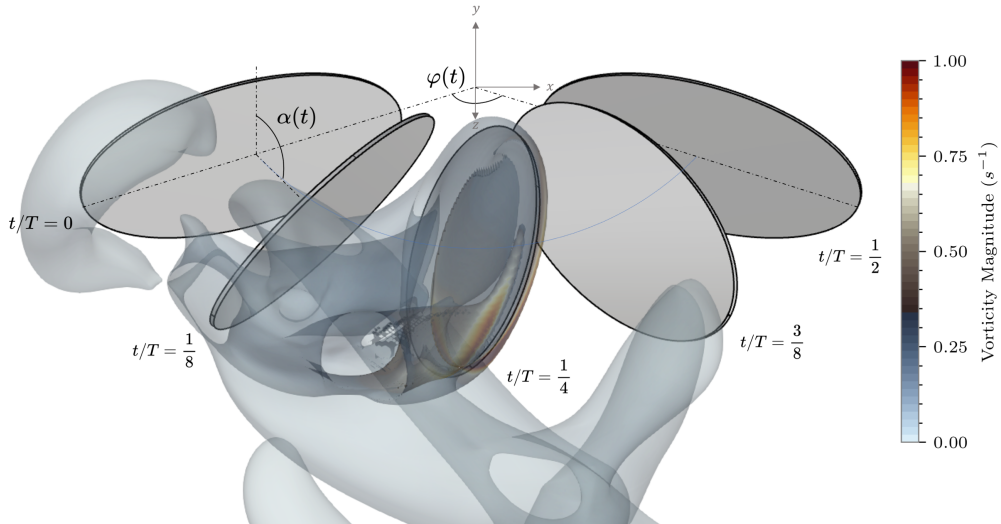
Figure 11: Elliptical plate wing at different time during an oscillatory period. Motion kinematics are: $f_r = 0.5$, $A_\theta = 0$, $A_\varphi = 0.35\pi$ and $A_\alpha = \pi/4$. The blue line represents the motion of the center of the wing. The vortical structures are shown as iso-surface of λ_2-criterion ($\lambda_2 U^2/D^2 = -8$) colored with vorticity magnitude ($\omega U/D$), shown only for $t/T = 1/4$. Animations of the above figure are provided as supplementary material.

405 an ellipsoid [34, 35, 36, 37, 38] defined by the following equation:

$$\frac{x^2}{a^2} + \frac{y^2}{b^2} + \frac{z^2}{c^2} = 1, \tag{28}$$

406 where $a = 0.5$, $b = 0.05$ and $c = 1$. However, to highlight the ability of
407 BDIM-σ to approach the true wing's geometry, we model the wing as an
408 elliptically-shaped and initially flat shell (*i.e.* a plate) with constant minimal
409 thickness d. Of course, the two representations match in the limit of $b \to 0$
410 and $d \to 0$, as the wing becomes an ellipsoidal flat plate.

The wing's motion is completely described by the three following Euler

angles

$$\varphi(t) = A_\varphi \cos(2\pi f_r t), \qquad (29a)$$

$$\theta(t) = A_\theta \sin(2\pi f_\theta t), \qquad (29b)$$

$$\alpha(t) = \frac{\pi}{2} - A_\alpha \sin(2\pi f_r t + \xi). \qquad (29c)$$

We set the flapping amplitude to $A_\varphi = 0.35\pi$ and the angle of attack amplitude to $A_\alpha = \pi/4$, see Figure 11, to replicate the numerical results presented in [37]. The deviation amplitude, A_θ is set to zero such that the flapping motion is constrained to the $x - z$ plane. The flapping and angle of attack frequencies are taken as $f_r = 0.5 \ Hz$. The deviation of the angle of attack to the flapping angle is set to zero $\xi = 0$. These kinematics result in a Rosby number of $Ro \equiv R_{tip}/\bar{c} = 3.2$ and a Reynolds number of $Re \equiv \bar{c}U/\nu = 100$, where R_{tip} is the distance from the instantaneous center of motion (in this case, the origin) to the tip of the wing and $\bar{c}$ is the mean chord of the wing. The reference velocity is defined as $U = f_r R_g \int_0^{1/f_r} \sqrt{\dot{\varphi}^2 + \dot{\theta}^2} \, dt$, and the radius of gyration $R_g = \sqrt{\frac{1}{S} \int_0^R c r^2 \, dr}$.

6.1. Numerical Method

A uniform grid region of $[2.6 \times 1.7 \times 1.8]$ wing span is used to properly capture the unsteady flow structures around the wing, see Figure 12. Grid stretching is used to fill the rest of the domain until it reaches the total size of $[8 \times 5.5 \times 5]$ wing span. A zero normal flux condition is applied on all exterior boundary of the domain. The no-slip boundary condition is applied to the immersed body.

Convergence is assessed using the mean lift coefficient over the last four periods (good periodicity is found for the last four period of motion of our
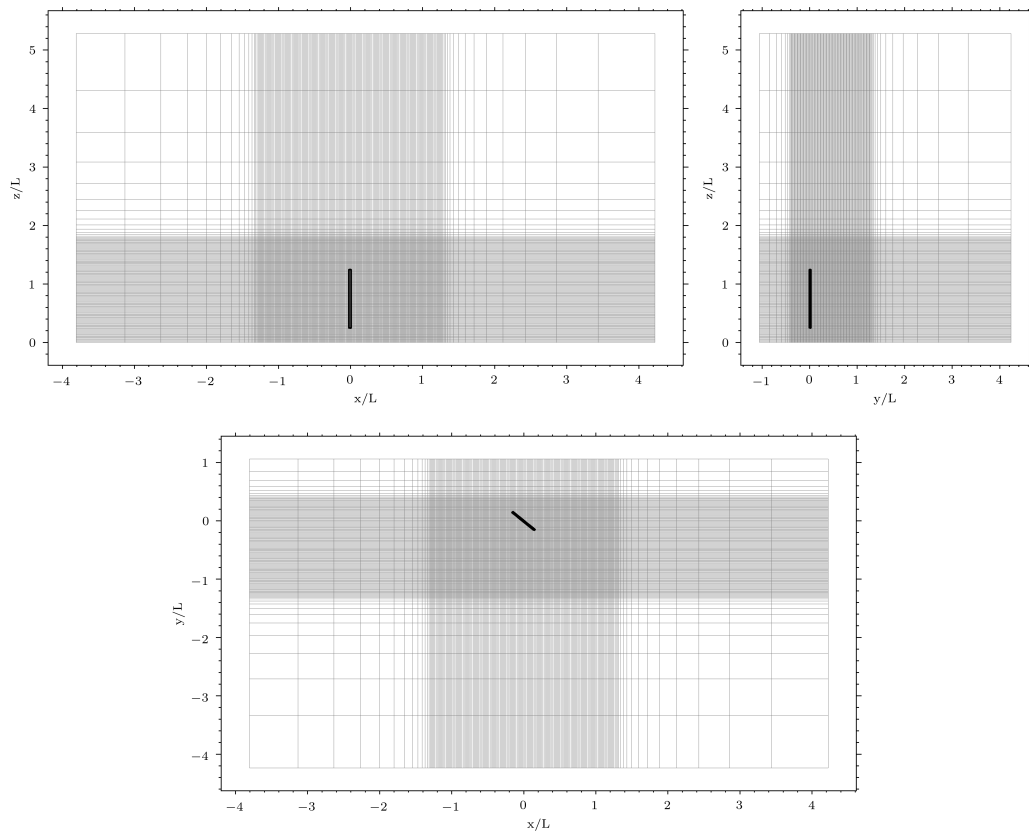
30

Figure 12: First-angle projection of the finest grid used for the ellipsoidal wing case. The wing is shown at $t/T = 0.25$. For clarity every two cells are shown in each direction.
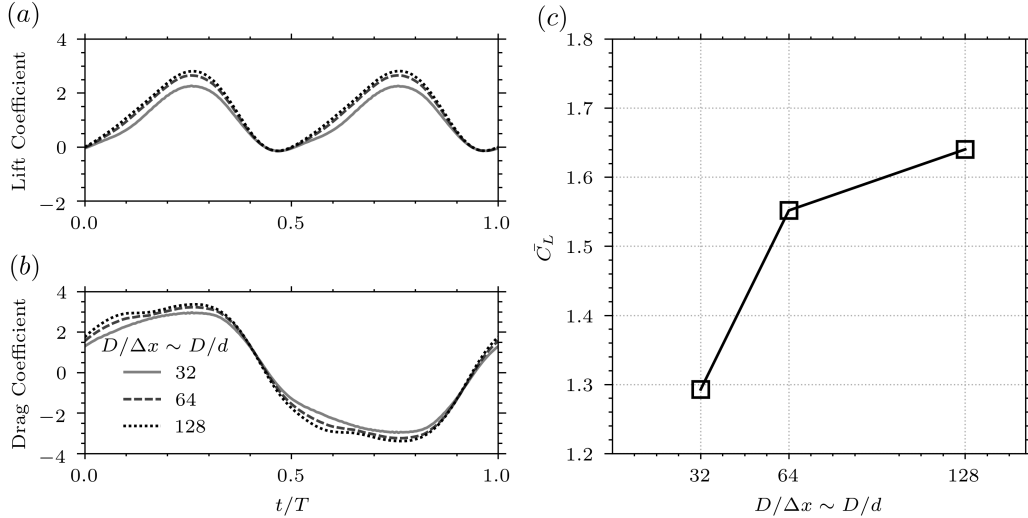
Figure 13: Geometrical sensitivity study of the (*a*) lift and (*b*) drag coefficient for the wing with the minimum body thickness $d = (1 + \sqrt{3})\Delta x$. (*c*) convergence of the mean lift coefficient for varying resolution and thicknesses.

system, see Figure 15d). We vary the resolution while using the thinnest possible body. The convergence rate with thickness is found to be $O((d/D)^{1.55})$ with relative error to the Richardson extrapolated value of 2.7% for the finest mesh, and so this is the mesh used in the results. As with the accelerating disk case, the convergence rate is less than 2 because the thickness is simultaneously reducing with Δx.

6.2. Results

Results are presented in terms of time dependent lift and drag coefficients

$$C_L = \frac{F_y}{\frac{1}{2}\rho U^2 S} \,, \qquad C_D = \frac{F_x \cos(\varphi) - F_z \sin(\varphi)}{\frac{1}{2}\rho U^2 S} \,, \tag{30}$$

where S is the surface area of the ellipsoidal wing and F_i is the ith component of the instantaneous force acting on the wing. We model the wing with the

32
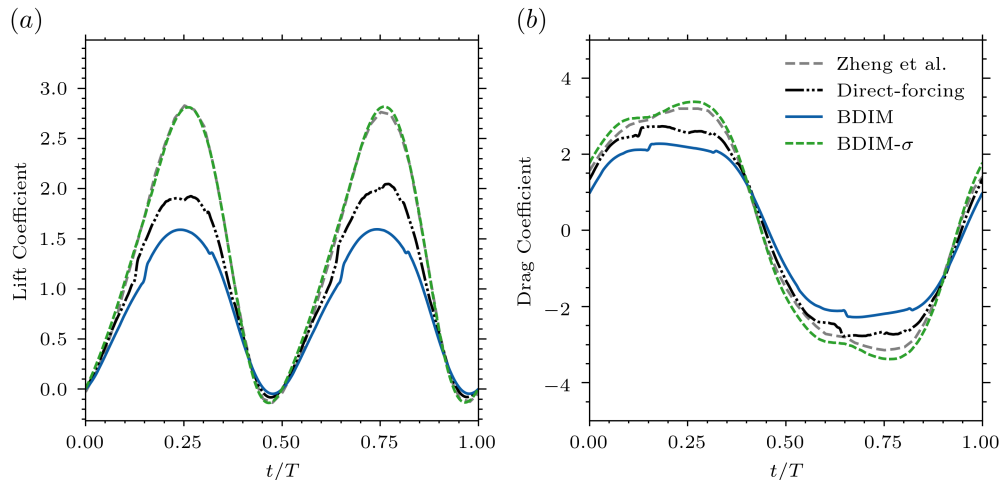
Figure 14: Time history of the (*a*) lift and (*b*) drag coefficient for the wing. Results are presented for a single period after the motion become independent of the initial conditions.

same thickness $d = (1 + \sqrt{3})$ for all the Immersed Boundary methods.

We include additional numerical results of the flow around an ellipsoidal wing obtained in Zheng et al. [37]. Despite the fact that [37] models the wing as a thin ellipsoid instead of an elliptical plate the lift and drag coefficient results are very comparable to BDIM-σ. The Direct-forcing and BDIM results shows a large under-prediction of the forces. Figure 15a-c shows that this large under-prediction is due to a different pressure field around the body. In the Direct-forcing method this pressure field is the result of the non-existant pressure boundary condition applied to the Poisson equation. Because the body is very thin, the standard BDIM method does not properly impose the pressure boundary condition either, which results in a leakage of fluid across the interface. This issue is resolved with our new method which allows the simulation of very thin membrane wings, bringing our simulation closer to real-life insects wings than the simplified ellipsoidal wing used in previous
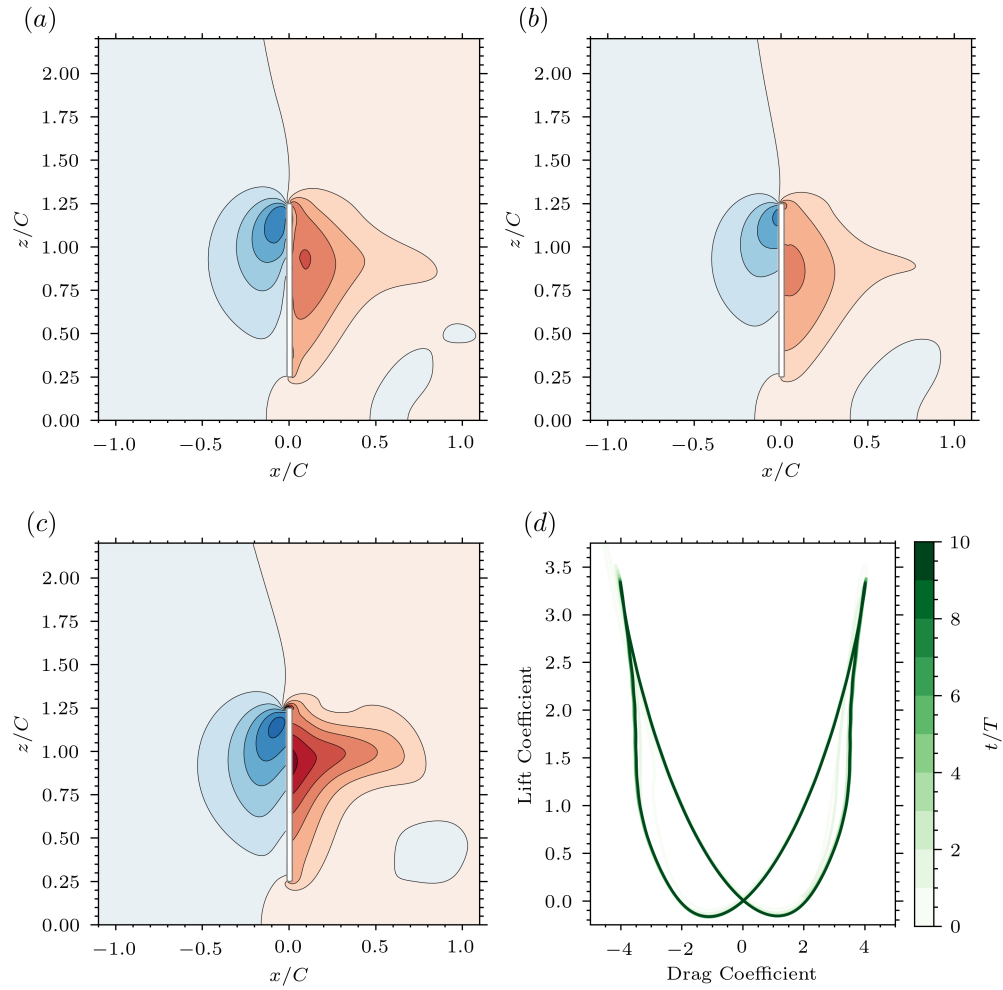
Figure 15: Pressure contour at $t/T = 0.25$ for the ellipsoidal wing with a thickness $(1 + \sqrt{3})\Delta x$ for (a) the Direct-forcing method (b) BDIM and (c) BDIM-σ. The 15 contour levels are evenly spaced between $c_p = \pm 7.0$. (d) Phase portrait of the wing forces for the BDIM-σ method. Clear periodicity is found for $t/T > 6$.

studies. As detailed in Appendix B, the reduced smoothing width ϵ used in BDIM-σ induces a small high-frequency numerical noise in the pressure force's temporal-spectra. However, the magnitude of the noise is still less than the Direct-forcing method, six orders of magnitude smaller than the low frequency physical signal, and does not corrupt the spatial pressure field, see Figure 15c.

Because the normal pressure gradient close to the immersed body doesn't match the local body acceleration, the Direct-forcing method and BDIM results in an error in the fluid velocity inside the body. We measure the error in the momentum flux of fluid through the wing's mid-plane, defined as

$$\text{error}_u \equiv \oint_{\sigma} (\vec{u} - \vec{v}_b) \cdot \vec{v}_b \, \mathrm{d}x_B, \tag{31}$$

where $\vec{v}_b$ is the body velocity, and σ is the surface representing the mid-plane of the ellipsoidal wing. We approximate this surface integral numerically by integrating over all cells that are located on the mid-plane of the body. In Direct-forcing methods, this error is only introduced in the projection step, and is not present in the intermediate velocity field, whereas it is already present in the intermediate velocity field in BDIM. The time variation of this error is shown on Figure 16. The large negative error observed represents a deficit in the local fluid velocity inside the body. This means that the forcing generated by the immersed surface is not properly radiated onto the fluid field, in agreement with the under-predicted lift and drag forces discussed above. A reversal of the sign of the error is observed just before the wing reaches the maximum flapping amplitude ($t/T = 0.5$ or $t/T = 1$).
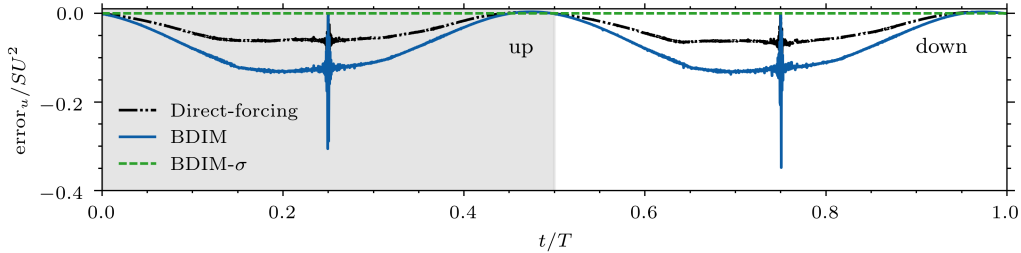
Figure 16: Time variation of the velocity error in Direct-forcing method, BDIM and the BDIM-σ for a single motion period. The gray in white shaded areas represent the up and down stroke, respectively. The surface integral over the mid-plane of the wing is normalized by the product of wing area and velocity magnitude squared SU^2. The L_∞-norm of the velocity error for the BDIM-σ for the period shown is 2.261×10^{-7}.

7. Conclusions

This manuscript provides analytical and numerical demonstration that most immersed boundary methods violate the pressure boundary condition for thin dynamic surfaces, resulting in a violation of the velocity boundary condition and erroneous flow fields and pressures forces. With the help of an illustrative one-dimensional problem, we show that the treatment of the pressure boundary condition in immersed boundary method is closely linked to the accuracy of the final velocity field, and that the magnitude of this error increases with Reynolds number. An analysis of the discretized pressure Poisson equation shows that in order to enforce the pressure boundary condition correctly the immersed boundary method must either solve an augmented system or modify the Poisson matrix coefficients such that the solution may be discontinuous across the boundary.

This analysis allows us to specify an extension of the original BDIM method to thin dynamic surface called BDIM-σ. This new method adjusts

36

the signed distance function to maintain a minimal body thickness that ensures proper imposition of the Neumann condition onto the body. The method relies on the slender-body notation to describe the mid-plane of the body with prescribed thickness. We note that this notation is commonly used to describe the kinematic of thin shells (see [25, 26], for examples) and therefore provides a link for possible use of this modified method for fluid-structure interaction problems involving thin flexible structures.

Challenging three-dimensional test cases demonstrate that the new BDIM-σ approach outperforms the Direct-forcing method and the original BDIM approach when dealing with thin dynamic bodies dominated by pressure forces, as is typical in many intermediate and high Reynolds number fluid-structure interaction problems. In particular, BDIM-σ always enforces the velocity and pressure boundary conditions on the surfaces regardless of resolution, ensuring accurate flow and force predictions compared to analytic solutions, previous high-resolution numerical studies, and experimental results.

The ability of the new BDIM-σ approach to deal with thin dynamic surfaces opens a wide range of exciting fluid-structure interaction applications such as sails, flexible insect wings, swimming fins, inflatable structures and many others. We believe that this approach will allow accurate and efficient flow simulations around highly dynamic non-linear shells and membranes.

8. Acknowledgements

Appendix A. Taylor-Green Vortex

We demonstrate the accuracy of the flow solver *without* an immersed body
by simulating the decay of a periodic vortex array on a domain $x, y \in [0, 1]$.
The decay of the velocity and pressure field is governed by

$$u(x, y, t) = \sin(k_x x) \cos(k_y y) \mathrm{e}^{-(k_x^2 + k_y^2)\nu t} \tag{A.1a}$$

$$v(x, y, t) = -\cos(k_x x) \sin(k_y y) \mathrm{e}^{-(k_x^2 + k_y^2)\nu t} \tag{A.1b}$$

$$p(x, y, t) = \frac{1}{4} \left(\cos(2k_x x) + \cos(2k_y y) \right) \mathrm{e}^{-(k_x^2 + k_y^2)\nu t} \tag{A.1c}$$

with $k_x = k_y = 2\pi$ and $\nu = 0.001$. This analytical solution to the Navier-
Stokes equation serves as initial condition for the simulations and exact solu-
tion from which we measure the error using the L-2 norm (see Equation 26).
We use four distinct mesh of size N^2 with $N \in [64, 128, 256, 512]$ and com-
pute the error at $t = 1s$ and compared to the analytical solution, results are
presented on Figure A.17a. Higher-than second-order convergence is found
for both the pressure and velocity field, demonstrating the spatial accuracy of
our solver. The temporal convergence is assessed using the finest mesh (512^2)
to keep spatial discretization error to a minimum and by gradually halving
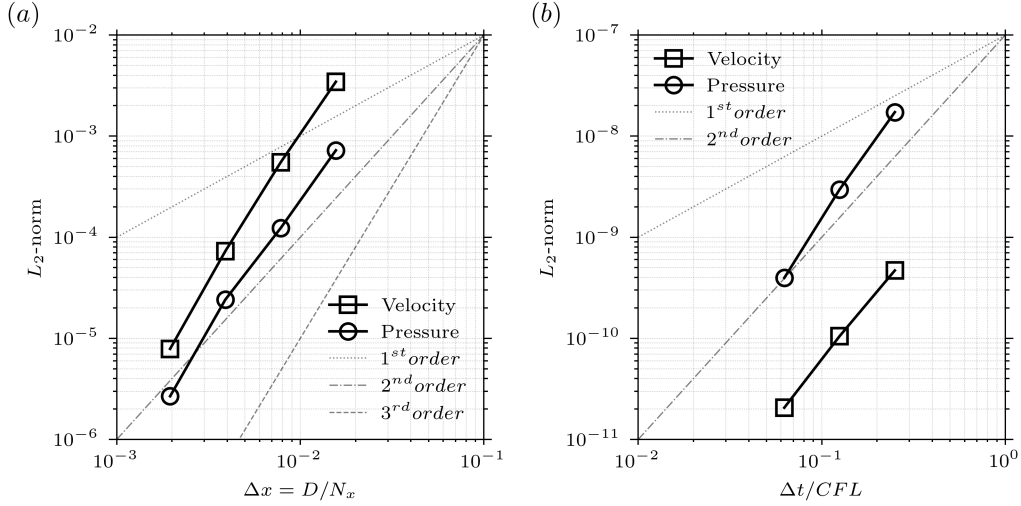the time-step/CFL ratio with $\Delta t / CFL \in [2, 4, 8, 16]$. Although the spatial

38

Figure A.17: (a) Spatial and (b) Temporal convergence of the flow solver on the 2D Taylor-Green vortex.

truncation error is small at this resolution (10^{-5}), it is orders of magnitude larger than the temporal truncation error. This does not allow to compare the solution obtained with various time-steps to the analytical solution. As such, we use the numerical simulation obtained with $\Delta t/CFL = 1/16$ as the *exact* solution and compute the error with reference to this result. Second-order convergence is found for the velocity field, with higher-than second-order convergence in the pressure field, see Figure A.17b.

Appendix B. Force Spectra

The spectral content of the lift and drag coefficient for the different methods are shown in Figure B.18. To remove the temporal noise in the force integral over the surface of the body, we use a high-frequency filter with a cuttoff frequency of $100\ Hz$.
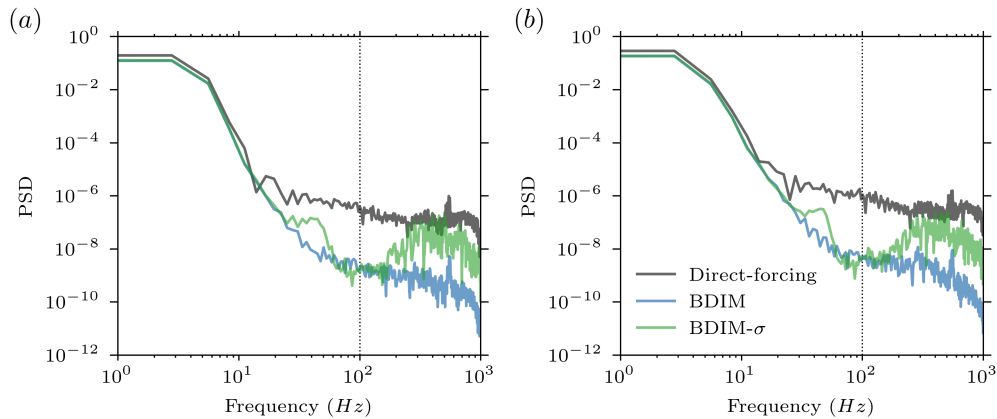
Figure B.18: Spectral density of the time-dependent lift (a) and drag (b) coefficient. We use a simple high-frequency filter to remove the noise above $100\ Hz$.

$$\tilde{C}_L(f) = \begin{cases} \tilde{C}_L(f) & \text{if } f < f_{\text{cutoff}}, \\ 0. & \text{else.} \end{cases} \tag{B.1}$$

References

[1] W. Kim, H. Choi, Immersed boundary methods for fluid-structure interaction: A review, International Journal of Heat and Fluid Flow 75 (2019) 301–309. doi:https://doi.org/10.1016/j.ijheatfluidflow.2019.01.010.

[2] B. E. Griffith, N. A. Patankar, Immersed Methods for Fluid – Structure Interaction, Annual Review of Fluid Mechanics (2020) 421–448. doi:https://doi.org/10.1146/annurev-fluid-010719-060228.

[3] R. Mittal, G. Iaccarino, Immersed Boundary Methods, Annual Review of Fluid Mechanics 37 (2005) 239–261. doi:https://doi.org/10.1146/annurev.fluid.37.061903.175743.

[4] C. S. Peskin, Flow patterns around heart valves: a numerical method, Journal of computational physics 10 (1972) 252–271. doi:https://doi.org/10.1016/0021-9991(72)90065-4.

[5] L. Zhu, C. S. Peskin, Simulation of a flapping flexible filament in a flowing soap film by the immersed boundary method, Journal of Computational Physics 179 (2002) 452–468. doi:https://doi.org/10.1006/jcph.2002.7066.

[6] C. S. Peskin, B. Feller Printz, Improved Volume Conservation in the Computation of Flows with Immersed Elastic Boundaries, Journal of Computational Physics 105 (1993) 33–46. doi:https://doi.org/10.1006/jcph.1993.1051.

[7] B. E. Griffith, On the volume conservation of the immersed boundary method, Communications in Computational Physics 12 (2012) 401–432. doi:https://doi.org/10.4208/cicp.120111.300911s.

[8] Y. Bao, A. Donev, B. E. Griffith, D. M. McQueen, C. S. Peskin, An Immersed Boundary method with divergence-free velocity interpolation and force spreading, Journal of Computational Physics 347 (2017) 183–206. doi:http://doi.org/10.1016/j.jcp.2017.06.041.

[9] J. Mohd-Yusof, Combined immersed-boundary/b-spline methods for simulations of flow in complex geometries, Center for Turbulence Research - Annual Research Briefs (1997). doi:https://doi.org/10.1006/jcph.2000.6484.

[10] E. A. Fadlun, R. Verzicco, P. Orlandi, J. Mohd-Yusof, Combined Immersed-Boundary Finite-Difference Methods for Three-Dimensional Complex Flow Simulations, Journal of Computational Physics 161 (2000) 35–60. doi:https://doi.org/10.1006/jcph.2000.6484.

[11] E. Balaras, Modeling complex boundaries using an external force field on fixed Cartesian grids in large-eddy simulations, Computers and Fluids 33 (2004) 375–404. doi:https://doi.org/10.1016/S0045-7930(03)00058-6.

[12] A. J. Chorin, The numerical solution of the Navier-Stokes equations for an incompressible fluid, Bulletin of the American Mathematical Society 73 (1967) 928–931. doi:https://doi.org/10.1016/0045-7930(73)90010-8.

[13] K. Taira, T. Colonius, The immersed boundary method: A projection approach, Journal of Computational Physics 225 (2007) 2118–2137. doi:https://doi.org/10.1016/j.jcp.2007.03.005.

[14] R. D. Guy, D. A. Hartenstine, On the accuracy of direct forcing immersed boundary methods with projection methods, Journal of Computational Physics 229 (2010) 2479–2496. doi:https://doi.org/10.1016/j.jcp.2009.10.027.

[15] T. Kempe, J. Fröhlich, An improved immersed boundary method with direct forcing for the simulation of particle laden flows, Journal of Computational Physics 231 (2012) 3663–3684. doi:https://doi.org/10.1016/J.JCP.2012.01.021.

[16] S. Gsell, J. Favier, Direct-forcing immersed-boundary method: A simple correction preventing boundary slip er-

ror, Journal of Computational Physics 435 (2021) 110265. doi:https://doi.org/10.1016/J.JCP.2021.110265.

[17] G. D. Weymouth, D. K. P. Yue, Boundary data immersion method for Cartesian-grid simulations of fluid-body interaction problems, Journal of Computational Physics 230 (2011) 6233–6247. doi:https://doi.org/10.1016/j.jcp.2011.04.022.

[18] A. P. Maertens, G. D. Weymouth, Accurate Cartesian-grid simulations of near-body flows at intermediate Reynolds numbers, Computer Methods in Applied Mechanics and Engineering 283 (2015) 106–129. doi:https://doi.org/10.1016/j.cma.2014.09.007.

[19] T. Colonius, K. Taira, A fast immersed boundary method using a nullspace approach and multi-domain far-field boundary conditions, Computer Methods in Applied Mechanics and Engineering 197 (2008) 2131–2146. doi:https://doi.org/10.1016/j.cma.2007.08.014.

[20] J. Blair Perot, An Analysis of the Fractional Step Method, Journal of Computational Physics 108 (1993) 51–58. doi:10.1006/JCPH.1993.1162.

[21] J. C. Strikwerda, Y. S. Lee, The Accuracy of the Fractional Step Method, SIAM Journal on Numerical AnalysisJ 37 (1999) 37–47. doi:https://doi.org/10.1137/S0036142997326938.

[22] D. L. Brown, R. Cortez, M. L. Minion, Accurate Projection Methods for the Incompressible Navier–Stokes Equations, Journal of Computational Physics 168 (2001) 464–499. doi:10.1006/JCPH.2001.6715.

[23] R. Bale, N. A. Patankar, N. Jansson, K. Onishi, M. Tsub-okura, Stencil Penalty approach based constraint immersed boundary method, Computers & Fluids (2020) 104457. doi:https://doi.org/10.1016/j.compfluid.2020.104457.

[24] M. Lauber, 1d-piston, https://github.com/marinlauber/Flexible-Sheets/tree/master/ 2020.

[25] L. Chen, N. Nguyen-Thanh, H. Nguyen-Xuan, T. Rabczuk, S. P. A. Bordas, G. Limbert, Explicit finite deformation analysis of isogeometric membranes, Computer Methods in Applied Mechanics and Engineering 277 (2014) 104–130. doi:https://doi.org/10.1016/j.cma.2014.04.015.

[26] T. X. Duong, F. Roohbakhshan, R. A. Sauer, A new rotation-free isogeometric thin shell formulation and a correspond-ing continuity constraint for patch boundaries, Computer Meth-ods in Applied Mechanics and Engineering 316 (2017) 43–83. doi:https://doi.org/10.1016/j.cma.2016.04.008.

[27] A. Gilmanov, F. Sotiropoulos, A hybrid Cartesian/immersed bound-ary method for simulating flows with 3D, geometrically complex, mov-ing bodies, Journal of Computational Physics 207 (2005) 457–492. doi:10.1016/j.jcp.2005.01.020.

[28] B. F. Garcia, G. D. Weymouth, V.-t. Nguyen, Span effect on the turbu-lence nature of flow past a circular cylinder, Journal of Fluid Mechanics 878 (2019) 306–323. doi:https://doi.org/10.1017/jfm.2019.637.

44

[29] J. N. Fernando, G. D. Weymouth, D. E. Rival, On the limits of added-mass theory in separated flows and with varying initial conditions, Journal of Fluids and Structures 93 (2020) 102835. doi:https://doi.org/10.1016/j.jfluidstructs.2019.102835.

[30] A. N. Zurman-Nasution, B. Ganapathisubramani, G. D. Weymouth, Influence of three-dimensionality on propulsive flapping, Journal of Fluid Mechanics 886 (2020) A25. doi:https://doi.org/10.1017/jfm.2019.1078.

[31] B. Leonard, A stable and accurate convective modelling procedure based on quadratic upstream interpolation, Computer Methods in Applied Mechanics and Engineering 19 (1979) 59–98. doi:https://doi.org/10.1016/0045-7825(79)90034-3.

[32] C. E. Brennen, A review of added mass and fluid inertial forces, BRENNEN (CE) SIERRA MADRE CA (1982).

[33] F. Kaiser, J. Kriegseis, D. E. Rival, The influence of edge undulation on vortex formation for low-aspect-ratio propulsors, Journal of Fluid Mechanics 883 (2020) A55. doi:https://doi.org/10.1017/jfm.2019.908.

[34] Z. J. Wang, J. M. Birch, M. H. Dickinson, Unsteady forces and flows in low Reynolds number hovering flight: Two-dimensional computations vs robotic wing experiments, Journal of Experimental Biology 207 (2004) 449–460. doi:https://doi.org/10.1242/jeb.00739.

[35] S. P. Sane, M. H. Dickinson, The control of flight force by a flapping wing: Lift and drag production, Journal of Experimental Biology 204 (2001) 2607–2626.

[36] F. M. Bos, B. W. van Oudheusden, H. Bijl, Wing performance and 3-D vortical structure formation in flapping flight, Journal of Fluids and Structures 42 (2013) 130–151. doi:https://doi.org/10.1016/j.jfluidstructs.2013.04.002.

[37] H. Zheng, F. Xie, T. Ji, Y. Zheng, Kinematic parameter optimization of a flapping ellipsoid wing based on the data-informed self-adaptive quasi-steady model, Physics of Fluids 32 (2020) 041904. doi:https://doi.org/10.1063/1.5144642.

[38] F. M. Bos, D. Lentink, B. W. Van oudheusden, H. Bijl, Influence of wing kinematics on aerodynamic performance in hovering insect flight, Journal of Fluid Mechanics 594 (2008) 341–368. doi:https://doi.org/10.1017/S0022112007009172.